Image-domain and data-domain waveform tomography: a case study

Esteban Díaz[1], Yuting Duan[1], Gerhard Pratt[2], and Paul Sava[1]
[1]*Center for Wave Phenomena, Colorado School of Mines*
[2]*University of Western Ontario*

ABSTRACT
Wavefield-based tomographic methods are idoneous for recovering velocity models from seismic data. The use of wavefields rather than rays is more consistent with the bandlimited nature of seismic data. Image domain methods seek to improve the focusing in extended images, thus producing better seismic images. However, image domain methods produce low resolution models due to the fact their objective functions are smooth, particularly in the vicinity of the global minimum. In contrast, data-domain methods produce high resolution models but suffer from strong non-linearity causing cycle skipping if certain conditions are not met. By combining the characteristics of each method, we can obtain models that produce better images and contain high resolution features at the same time. We demonstrate the strength of the workflow that combines both methods with an application to a marine 2D dataset with variable streamer depth.

Key words: Wavefield tomography

1 INTRODUCTION

An accurate velocity model is the main requirement for a successful imaging. In order to be consistent with the typical band-limited seismic data, one ought to use wavefield-based tomographic. The wavefield-based approach avoids shortcomings inherent in ray-based methods, such as limited model sensibility (a ray travels trough a infinitesimally narrow path inside the model) and instability around sharp boundaries in the velocity model.

Velocity analysis methods based on wavefield extrapolation are commonly referred to as Wavefield Tomography (WT) (Tarantola, 1984; Woodward, 1992; Pratt, 1999; Sava and Biondi, 2004a,b; Shen and Symes, 2008; Biondi and Symes, 2004; Symes, 2008) ; such tomographic approaches can be formulated either in the image domain, where one tries to improve image quality, or in the data domain, where one seeks consistency between modeled and observed data.

Image-domain wavefield tomography can be formulated by many means. A common approach aims to improve the flatness of angle gathers, or equivalently one can improve the focusing of space-lag gathers (Shen and Calandra, 2005). Space-lag gathers (Rickett and Sava, 2002; Sava and Fomel, 2006), also referred to as sub-surface offset gathers, measure the spatial similarity between source and receiver wavefields. Hence, during tomography, one seeks to increase the similarity of the spatial correlation for a collection of seismic experiments (Shen and Symes, 2008; Yang and Sava, 2011; Weibull and Arntsen, 2013; Yang et al., 2013; Shan and Wang, 2013). Inverse problems formulated in the image domain are generally better-posed than those formulated in the data domain. This results from the fact that the image domain objective functions are smoother than those in the data domain.

Data-domain wavefield tomography is generally formulated by improving the consistency between modeled and observed data. Originally, Tarantola (1984) introduced the data difference as a similarity estimate in the time domain. Alternatively, the problem can be solved in the frequency domain (Pratt, 1999). Contrary to the image-domain formulation, data-domain wavefield tomography is highly non-linear i.e. the objective function has many local minima. To overcome the non-linearity, a multi-scale separation approach is needed (Bunks et al., 1995). Within each scale (frequency or frequency band), the problem can be more linear if the initial model is closer to the one corresponding to the global minimum. Another loop of multi-scale can be added by introducing time damping, a method commonly referred to as Laplace-Fourier waveform inversion (Sirgue and Pratt, 2004; Shin and Ho Cha, 2009). The purpose of the time damping is to fit earlier arrivals first, and then to fit later arrivals progressively.

Both data-domain and image-domain tomographic methods share many parts of the process: both use the same extrapolation engine (the two-way wave equation), and share similarities in building the gradient of the objective func-

tion through the Adjoint State Method framework (Tarantola, 1984; Plessix, 2006; Symes, 2008). In this report, we combine image-domain and data-domain wavefield tomography approaches for optimizing the velocity model. The idea is to produce a model that improves focusing with image-domain wavefield tomography and then refine it using data-domain wavefield tomography. We apply the wavefield tomography workflow to a marine 2D dataset. The data are acquired with a variable depth streamer cable, which produces a varied notch spectrum. The increasing depth produces a better low frequency response, which can be useful in the multi-scale approach discussed earlier.

2 IMAGE DOMAIN WAVEFIELD TOMOGRAPHY

In this section, we review the image-domain wavefield tomography using space-lag gathers (Rickett and Sava, 2002; Sava and Vasconcelos, 2011). These kind of gathers highlight the spatial consistency between wavefields by exploring the focusing information in the image domain. The moveout in the gather is sensitive to velocity perturbations, and hence can be optimized. Space-lag gathers are defined as follows:

$$R(\mathbf{x},\boldsymbol{\lambda}) = \sum_e \sum_t u_s(e,\mathbf{x}-\boldsymbol{\lambda},t)u_r(e,\mathbf{x}+\boldsymbol{\lambda},t), \quad (1)$$

where $\boldsymbol{\lambda}$ is the space-lag vector, $\mathbf{x}$ the image location, e the experiment index, u_s the source wavefield, and u_r the receiver wavefield. The source wavefield u_s is produced by forward extrapolation of the source function, whereas the receiver wavefield u_r is produced by backward propagation of the data at the receiver location. In matrix notation, the process is described by

$$\begin{bmatrix} \mathcal{L}(m,t) & 0 \\ 0 & \mathcal{L}^\top(m,t) \end{bmatrix} \begin{bmatrix} u_s \\ u_r \end{bmatrix} = \begin{bmatrix} f_s \\ f_r \end{bmatrix}, \quad (2)$$

where $m = 1/v^2(\mathbf{x})$ is the medium slowness squared, f_s is the source function, f_r is the data at the receiver locations, $\mathcal{L}(m)$, and $\mathcal{L}^\top(m)$ are forward and backward wave propagators, respectively. In this report we use the scalar wave equation as wave operator:

$$\mathcal{L}(m) = m(\mathbf{x})\frac{\partial^2}{\partial t^2} - \nabla^2. \quad (3)$$

A well-focused gather concentrates most of its energy around $\boldsymbol{\lambda} = 0$. This can be used as an optimization criterion by minimizing the energy outside $\boldsymbol{\lambda} = 0$. We can accomplish this by defining an objective function

$$J = \frac{1}{2}\left|\left|P(\boldsymbol{\lambda})R(\mathbf{x},\boldsymbol{\lambda})\right|\right|^2, \quad (4)$$

where $P(\boldsymbol{\lambda})$ is the penalty function, which plays a vital role in the inversion. Shen and Symes (2008) propose a mix between $P(\boldsymbol{\lambda}) = |\boldsymbol{\lambda}|$ and $P(\boldsymbol{\lambda}) = \delta(\boldsymbol{\lambda})$. The first penalty function corrects for most kinematic errors, whereas the second one improves the focusing of the image $R(\mathbf{x},\boldsymbol{\lambda} = \mathbf{0})$. Yang et al. (2013) propose a penalty operator $P(\boldsymbol{\lambda})$ that accounts for illumination, which seeks to bring the defocused data, not to $\boldsymbol{\lambda} = 0$, but to a region of acceptable focusing within the limits of illumination. Depending on the choice of the the penalty operator $P(\boldsymbol{\lambda})$, equation 4 can be either minimized or maximized. In this report, we use $P(\boldsymbol{\lambda}) = |\boldsymbol{\lambda}|$ as penalty operator primarly for computational cost reasons. This penalty operator defines a smooth objective function and corrects for most kinematic errors in the model.

Once we have the penalized gathers (image residuals), we compute the adjoint sources (Shen and Symes, 2008; Weibull and Arntsen, 2013),

$$g_s(\mathbf{x},t) = \sum_{\boldsymbol{\lambda}} P(\boldsymbol{\lambda})^2 R(\mathbf{x}+\boldsymbol{\lambda},\boldsymbol{\lambda})u_r(\mathbf{x}+2\boldsymbol{\lambda},t) \quad (5)$$

for the source adjoint source, and

$$g_r(\mathbf{x},t) = \sum_{\boldsymbol{\lambda}} P(\boldsymbol{\lambda})^2 R(\mathbf{x}-\boldsymbol{\lambda},\boldsymbol{\lambda})u_s(\mathbf{x}-2\boldsymbol{\lambda},t) \quad (6)$$

for the receiver adjoint source.

Yang and Sava (2010) and Shan and Wang (2013) use an alternative formulation for the source side:

$$\text{for all } \boldsymbol{\lambda}, \text{ do: } g_s(\mathbf{x}-\boldsymbol{\lambda},t) += P(\boldsymbol{\lambda})^2 R(\mathbf{x},\boldsymbol{\lambda})u_r(\mathbf{x}+\boldsymbol{\lambda},t), \quad (7)$$

and for the receiver side:

$$\text{for all } \boldsymbol{\lambda}, \text{ do: } g_r(\mathbf{x}+\boldsymbol{\lambda},t) += P(\boldsymbol{\lambda})^2 R(\mathbf{x},\boldsymbol{\lambda})u_s(\mathbf{x}-\boldsymbol{\lambda},t). \quad (8)$$

It turns out that both formulations are equivalent. In the first formulation, we gather information from the vicinity of position $\mathbf{x}$, whereas in the second one we scatter the residual in the vicinity of $\mathbf{x}$. In order to get the equivalence between equations 5 and 7 we can simply do a change of variables $\mathbf{x}' = \mathbf{x} - \boldsymbol{\lambda}$ in equation 7. Similarly, we can do the change of variables $\mathbf{x}' = \mathbf{x} + \boldsymbol{\lambda}$ in equation 8 to obtain the equivalence between equations 6 and 8.

Once we have the adjoint sources, we solve

$$\begin{bmatrix} \mathcal{L}^\top(m,t) & 0 \\ 0 & \mathcal{L}(m,t) \end{bmatrix} \begin{bmatrix} a_s \\ a_r \end{bmatrix} = \begin{bmatrix} g_s \\ g_r \end{bmatrix}. \quad (9)$$

The gradient of equation 4 with respect to our model parameters is defined as follows:

$$\nabla J(\mathbf{x}) = \sum_e \sum_t \ddot{u}_s(e,\mathbf{x},t)a_s(e,\mathbf{x},t) + \ddot{u}_r(e,\mathbf{x},t)a_r(e,\mathbf{x},t). \quad (10)$$

3 DATA DOMAIN WAVEFIELD TOMOGRAPHY

The construction of the tomography problem in the data domain amounts to measuring the error (or residual) at the receiver locations. For data domain wavefield tomography, we normally use the data difference for the residual:

$$J = \frac{1}{2}\left|\left|u_s(\mathbf{x}_r,\Omega) - f_r(\mathbf{x}_r,\Omega)\right|\right|^2 = \frac{1}{2}\left|\left|\Delta d\right|\right|^2, \quad (11)$$

where $\mathbf{x}_r$ are the receiver locations and Ω is the complex valued frequency whose purpose we will explain later. Note that

$f_r(\mathbf{x}_r, \Omega) = u_r(\mathbf{x}_r, \Omega)$. Since for building the residual we only need to forward propagate the source function

$$\mathcal{L}(m, \Omega)u_s = f_s(\mathbf{x}_s, \Omega), \tag{12}$$

we have to compute one adjoint wavefield $a_s(\mathbf{x}, \Omega)$. For data-domain wavefield tomography, computing a_s involves back-propagating the data residual:

$$\mathcal{L}^{\top}(m, \Omega)a_s = (\Delta d)^*. \tag{13}$$

Here $(\Delta d)^*$ is the complex conjugate residual and $\mathcal{L}(m, \Omega)$ is the acoustic wave equation in the frequency domain, defined as follows:

$$\mathcal{L}(m) = -\nabla \cdot \frac{1}{\rho(\mathbf{x})}\nabla - \frac{m(\mathbf{x})}{\rho(\mathbf{x})}\Omega^2. \tag{14}$$

Here $\rho(\mathbf{x})$ is the density of the medium. In this report, we do not invert for $\rho(\mathbf{x})$, instead we parametrize it as a function of the velocity following Gardner et al. (1974).

Once we obtain $u_s(\mathbf{x}, \Omega)$ and $a_s(\mathbf{x}, \Omega)$, we can proceed to compute the gradient:

$$\nabla J(\mathbf{x}) = \mathbb{R}\left\{\sum_e \sum_t \Omega^2 u_s(e, \mathbf{x}, \Omega)a_s^*(e, \mathbf{x}, \Omega)\right\}, \tag{15}$$

here * denotes complex conjugate and $\mathbb{R}\{\}$ denotes the real part.

The data domain wavefield tomography objective function, equation 11, is highly non-linear if we operate with signals in the normal frequency band. Hence, in order to increase the chances of convergence to the global minimum, it is customary to implement the data-domain wavefield tomography in a multi-scale fashion. Bunks et al. (1995) propose to first invert lower frequencies and then move gradually to higher frequencies. The idea is that within each scale the problem looks more linear than when inverts all the bandwidth at once.

An additional outer loop in the inversion is the time damping, which leads to the so-called Laplace-Fourier domain FWI (Sirgue and Pratt, 2004; Shin and Ho Cha, 2009). The purpose of this outer loop is to first fit earlier arrivals, and then fit later arrivals. By fitting first early arrivals (shorter travel-time) we reduce the risk of large phase differences between observed and modeled data which can cause cycle-skipping. Once the travel-time differences are solved for early arrivals, we can progressively increase τ. Introducing the time damping requires the following transformation: $\Omega = \omega + i/\tau$, with τ being the time damping (Kamei et al., 2013). Thus, this transformation turns the real-valued angular frequency ω into a complex-valued angular frequency Ω. In order to get consistent observed data with the damped modeled data, one must also scale the observed data as $f_r(\mathbf{x}_r, t) = d_{obs}(\mathbf{x}_r, t)e^{-t/\tau}$ before the transformation to frequency domain.

The low frequencies of the data are sensitive to the long wavelength (smooth) components of the earth model. However, if the data do not have such frequencies, data-domain wavefield tomography is unable to update such components. In contrast, focusing in extended images is mostly sensitive to the smooth components of the model. By implementing a joint workflow using image-domain wavefield tomography for updating the smooth components of the model and later using data-domain wavefield tomography for the high resolution features of the model, we can obtain a more complete spectrum in the model. The first pass using image-domain wavefield tomography has the ability to stabilize the cycle-skipping problems in data-domain wavefield tomography.

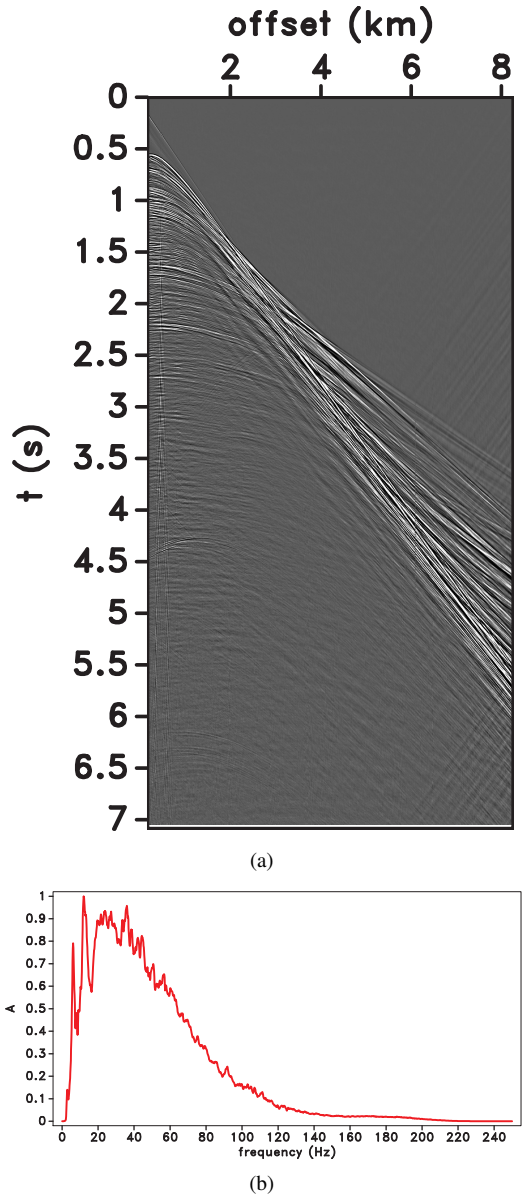


Figure 1. (a) Shot gather at $x = 14$ km and (b) its average amplitude spectrum.

4 APPLICATION TO A REAL 2D DATASET

In this section we apply the cascaded workflow of image-domain wavefield tomography followed by data-domain wave-

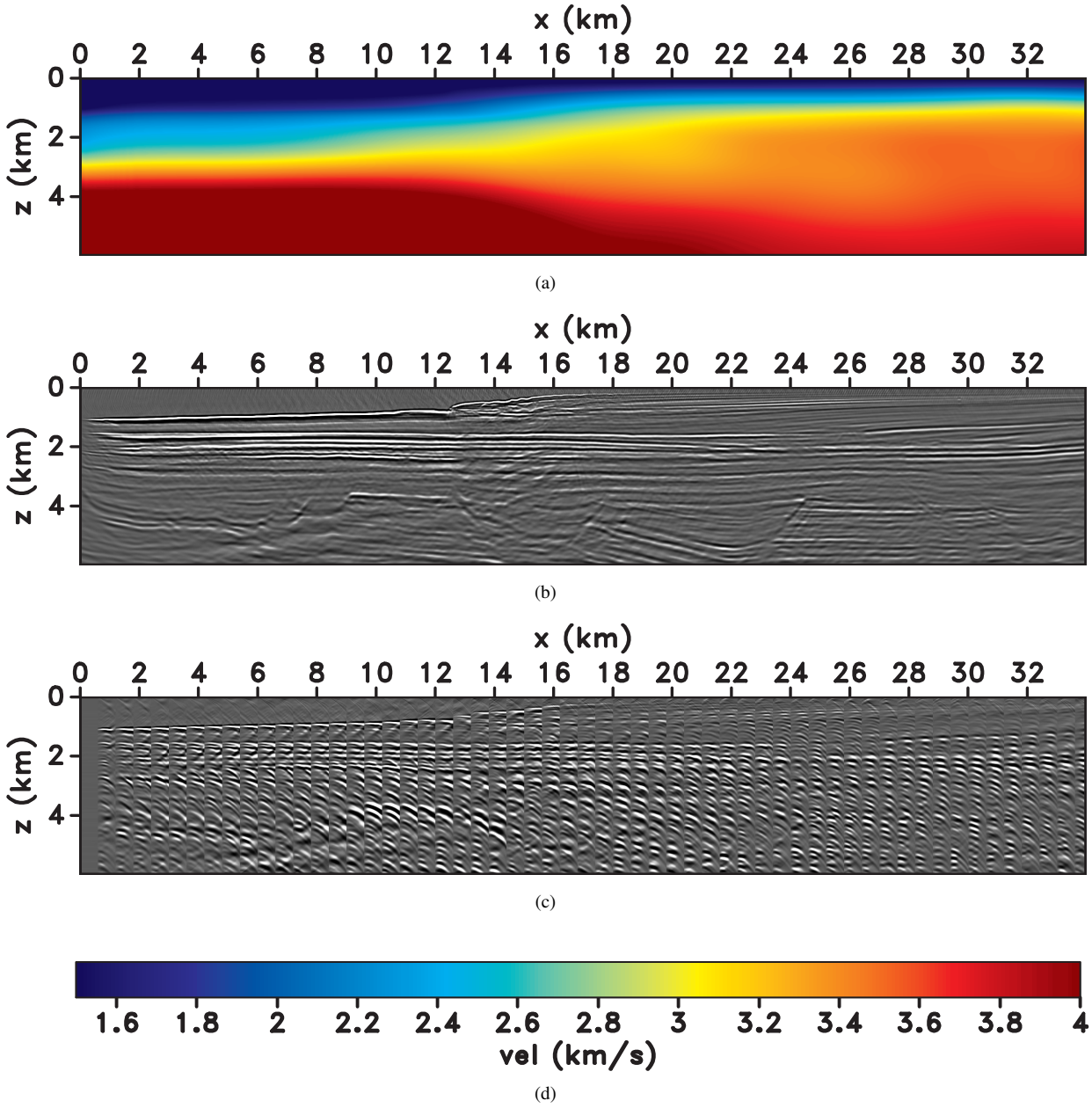


Figure 2. (a) Initial velocity model, (b) corresponding RTM image, (c) angle-gathers at sparse locations, and (d) the colorbar for velocity plots used in this report.

field tomography. We use image-domain wavefield tomography to correct for most kinematics errors, and then data-domain wavefield tomography to refine the model and add details. We compare 4 models: (a) the initial model, (b) the model obtained by image domain wavefield tomography, (c) the data-domain wavefield tomography obtained from (a), and (d) the data-domain wavefield tomography starting with the model obtained by image-domain wavefield tomography (b).

The dataset is a marine 2D line acquired with a variable depth cable. The towed streamer contains increasing depths as a function of offset, which enhances the frequency content of the data by producing a mixed notch response. Hence, the increased cable depths improves the low frequency content at intermediate and far offsets which can be very helpful for data-domain wavefield tomography. The cable contains offsets ranging from 0.169 to 8.256 km. Figure 1(a) shows a shot gather from $x = 14$ km and Figure 1(b) depicts the average amplitude spectrum for the same gather.

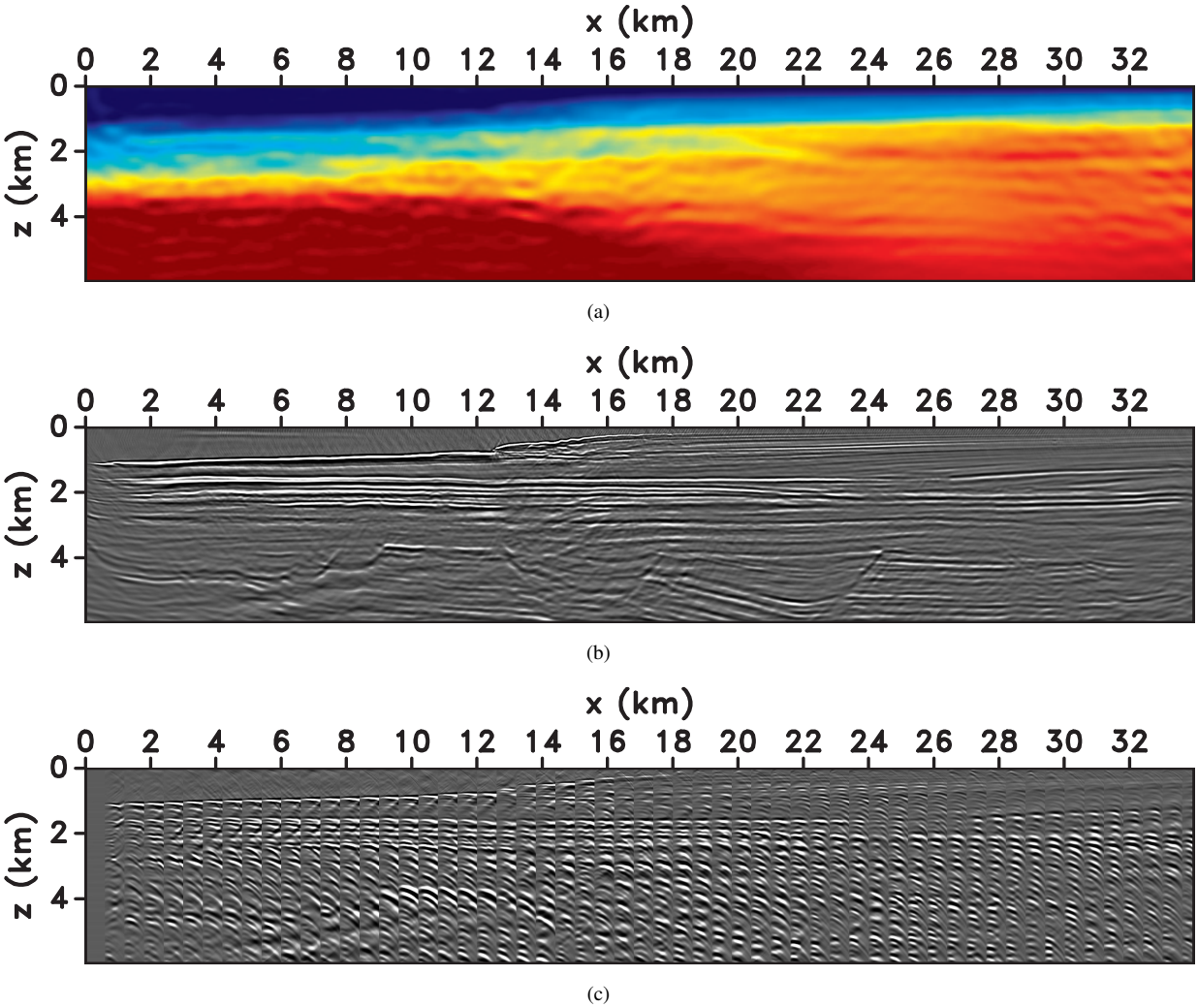


Figure 3. (a) The data-domain wavefield tomography velocity model obtained from Figure 2(a), (b) corresponding RTM image, and (c) angle-gathers at sparse locations. The velocity ranges from 1.5km for water velocity to 4km/s in the deepest part.

We build the initial model, Figure 2(a), by performing time-domain NMO analysis followed by smoothing, RMS (stacking) conversion to interval velocity (Dix, 1955), and time to depth conversion. Figure 2(b) shows the RTM image produced by the model in Figure 2(a), and one can observe that the image is over migrated (high velocity) below 3km in depth. Figure 2(c) shows angle gathers extracted at sparse locations in the model. Note that we do not use the angle gathers for inversion; instead, we use the gathers as an independent quality control tool. The transformation from space-lag gathers $R(\mathbf{x}, \boldsymbol{\lambda})$ to angle domain $R(\mathbf{x}, \theta)$ follows the method of Sava and Fomel (2003). The angles vary from 0 to 45° for all the gathers shown in this report. The moveout in the gathers confirms that the velocity is too fast below 3 km. Some of the events in the gathers, however, correspond to migrated surface related multiples and their moveout is not indicative of velocity error.

For data-domain wavefield tomography, we use 7 frequency blocks with 5 frequencies each. The center frequency for each block ranges from $f = 2.6$ Hz to $f = 8.9$ Hz. For the time damping constant, we use $\tau = 1.6s$. The first step in data domain wavefield tomography involves estimating the source function $f_s(\Omega)$; later we compare the inverted source functions for each model. We use 365 shots for the inversion with a shot interval $\Delta s = 0.09375$ km. The data-domain wavefield tomography workflow is common for the two inversions.

Figure 3(a) shows the data-domain wavefield tomography model built from Figure 2(a). The data-domain wavefield tomography process slows the velocity in the shallow part of the section, close to the water bottom, introducing a sharp discontinuity in the model. In general, the velocity slows down in the right part of the model. One can see in the gathers, Figure 3(c), that in the shallow part the events get flatter with the new velocity. However, deep in the section, the model does

not correct most kinematic problems exhibited in the gathers. This area of the model corresponds to longer travel-times in the data, and these late arrivals are prone to cycle-skipping problems.

We generate the model in Figure 4(a) using the image-domain wavefield tomography approach. The idea of this tomographic step is to correct for the bulk of the kinematic errors in the model. Figure 4(a) shows that in the updated model, in general the model slows down, especially in the deep part of the section. Figure 4(b) shows the corresponding RTM image, where the focusing of the image improves significantly around $z = 3.5$ km. This observation is confirmed in Figure 4(c), where now the gathers are flatter throughout the section.

Finally, we update the image-domain wavefield tomography model with the data-domain wavefield tomography approach. Figure 5(a) depicts the updated model (compare with Figure 3(a)), which changes considerably in the interval $z = 4$ km to $z = 6$ km. Figures 5(b)-5(c) are the corresponding RTM image and angle gathers, respectively. Note that even though the velocity does not significantly vary the kinematics of the experiment, it introduces subtle structural features in the image. We can see that the structure of the line becomes flatter with the new model (see for instance the event at $z = 4$ km and $x = 18$ to 24 km).

5 DISCUSSION

In the previous section we show the imaging results from different velocity models. In this section we do a quantitative comparison between the inverted models. Figures 3(a), 4(a), and 5(a) show that the right part of the model, $x > 14$ km, does not change significantly. However, we can see in both data-domain wavefield tomography models that the shallow part of the right side of the model improves the flatness of the gathers at shallow depths (compare Figure 2(c) with Figure 3(c)).

The image-domain wavefield tomography model (Figure 4(a)) does not significantly change the kinematics on the right side of the model. We can think of two reasons for this observation: (i) the right side of the model has poorer illumination, which can be confirmed by the limited angle range in the gathers, and (ii) given that the right side of the section has a shallower water column, then we can expect several orders of surface related multiples. We can address (i) by relaxing the mute in the input shot gathers and thus improving the illumination. Another option is to use a penalty operator $P(\boldsymbol{\lambda})$ that takes into account the spatially-variable illumination of the data, as suggested by Yang et al. (2013). In relation to point (ii), the presence of multiples (surface-related or internal) violates the implicit single scattering assumption of conventional and extended images. Weibull and Arntsen (2013) suggest creating data that conform to single scattering by muting the multiples in the extended images and then demigrate the gathers. This new dataset should remove the bias of the surface related multiples in the inversion. Another option is to demultiple the data prior to inversion (e.g. SRME (Verschuur et al., 1992)). All these improvement ideas remain for ongoing and future tests.

On the left side of the section we see significant changes. Figures 6(a) to 6(d) show a detailed view of the models for $x < 14$ km. The data-domain wavefield tomography model in Figure 6(d), built from from the initial model, shows some layering below the water bottom, where we can see a clear boundary in the model that is probably related to the events ranging from $z = 1.5$ km and $z = 2.5$ km. Given that the velocity is too fast, the data-domain wavefield tomography model is probably trapped in a local minimum. Hence, it cannot correct for the kinematic errors in the model. This is confirmed in the moveout of the gathers, shown in Figures 7(a)-7(b). There are not many differences to recognize from Figures 8(a)-8(b). This confirms that the data-domain wavefield tomography model did not alter the kinematics.

In contrast, when we compare previous models with the image-domain wavefield tomography model, Figure 6(c), we can appreciate a considerable correction to the velocity. Now, the slower velocity corrects for the bulk of the kinematic errors in the model. Figure 7(b) shows flat events up to $z = 4.5$ km through the detailed section. The new velocity highlights the unconformity depicted by the bright seismic event around $z = 4$ km. Also, we can see how new events get imaged between $z = 2.5$ km and $z = 4$ km in Figure 8(c). The updated model from data-domain wavefield tomography, depicted in Figure 6(d), now shows a sharp discontinuity in the velocity at $z = 3$ km. The corresponding image, Figure 8(d), shows a flatter structure after the data-domain wavefield tomography update. This is interesting because we can see how despite the added complexity in the velocity, the structure in the image is simplified.

Figures 9(a)-9(d) show the inversion of source functions for the initial, the data-domain wavefield tomography from the initial model, the image-domain wavefield tomography model, and the final data-domain wavefield tomography model, respectively. Note that the source functions inverted with the smooth model are laterally consistent. However, the consistency is improved in Figure 9(c). If we compare the source inversions from data-domain wavefield tomography models (Figures 9(b)-9(d)), we can see a higher lateral correlation, which confirms that the final data-domain wavefield tomography models better explain the kinematics of the data for direct and diving wave arrivals. Even though we invert each source individually, we use the average over source positions for the inversion. This is done because we know that in the field the air gun is shot with a constant pressure. Hence, we assume that the inconsistencies in the source functions come from the model itself.

Analyzing the focusing in space-lag gathers, or flatness of angle gathers, is the proper quality control tool for image-domain methods. The equivalent tool for data-domain methods are the data residuals. Figures 10(a)-10(d) show the time-domain data residuals for the four models discussed in this report for a shot gather at $x = 18.75$ km. Figure 10(a) shows the data residual corresponding to Figure 2(a). One can observe large amplitude and phase residuals trough the diving-waves components of the data. After updating the model the residual depicted in Figure 10(b) shows that the diving waves

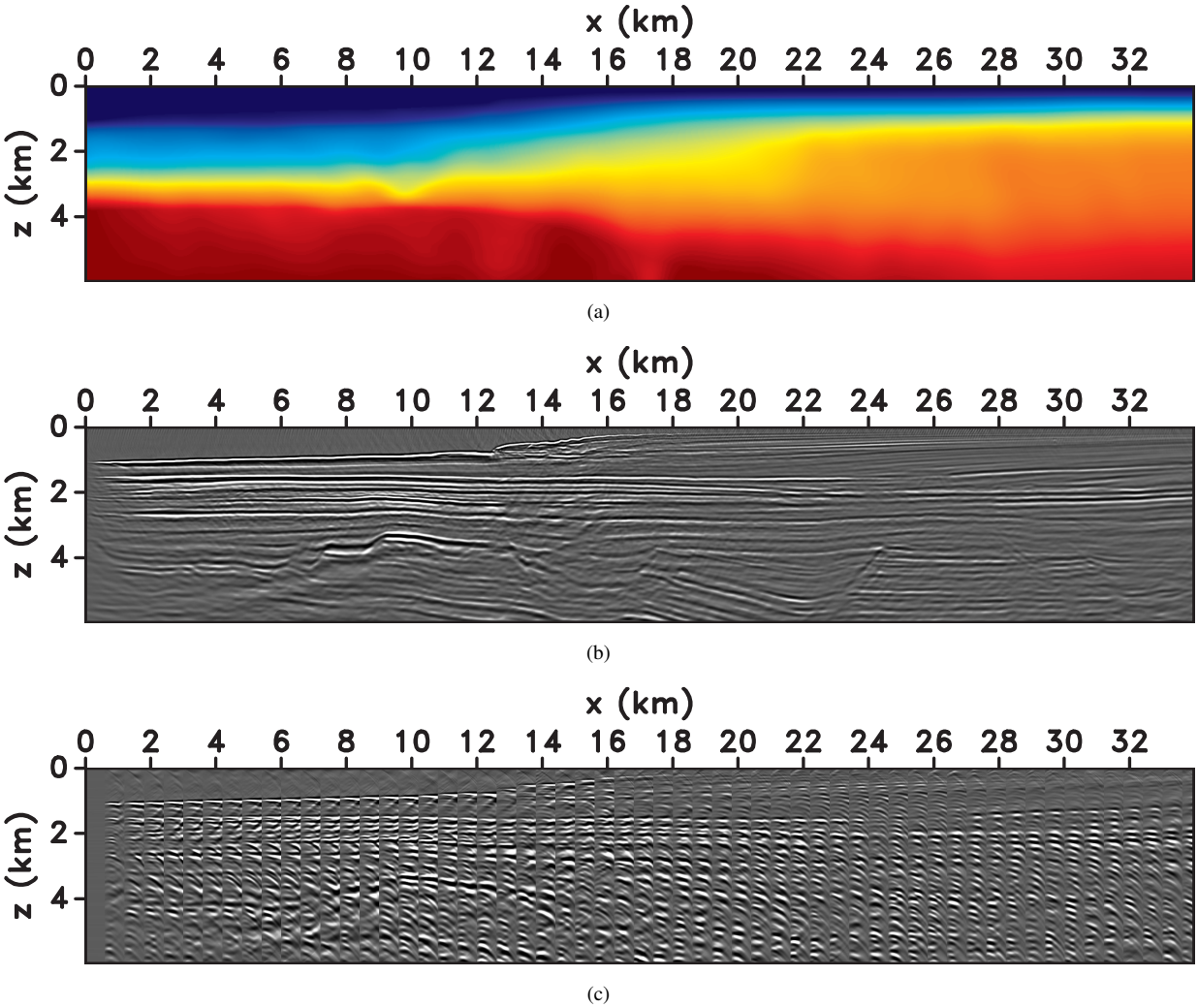


Figure 4. (a) The image-domain wavefield tomography velocity model built from Figure 2(a), (b) corresponding RTM image, and (c) angle-gathers at sparse locations. The velocity ranges from 1.5km for water velocity to 4km/s in the deepest part.

arrivals are better fit, specially between offsets 2.5 to 5 km. Figure 10(c) shows the residual corresponding to Figure 4(a), we can see that the these residuals better explain the data than those in Figure 10(a). After updating the model, Figure 10(d) we can see how the residuals from Figure 5(a) better fit the data than any of the previous models. Now, the direct arrivals have a good match for near and intermediate offsets.

6 CONCLUSIONS

The combination between image-domain and data-domain wavefield tomography seeks to exploit the features of each method. The image-domain wavefield tomography methods are sensitive to the smooth components of the model due to the definition of the inverse problem. Once we obtain a smooth model that improves focusing in the extended images, we can proceed to further refine the model using data-domain wavefield tomography. We demonstrate the cascaded workflow using a real 2D marine dataset. Our image-domain wavefield tomography model corrects for most kinematic errors in the model, whereas the data-domain wavefield tomography model corrects early arrival phase errors in the data, and introduces discontinuities in the model directly correlated with events in the image.

7 ACKNOWLEDGMENTS

We thank sponsor companies of the Consortium Project on Seismic Inverse Methods for Complex Structures. The seismic data shown in this report is proprietary to and provided courtesy of CGG. We thank Bruce VerWest for the support with the dataset. The reproducible numeric examples in this paper use

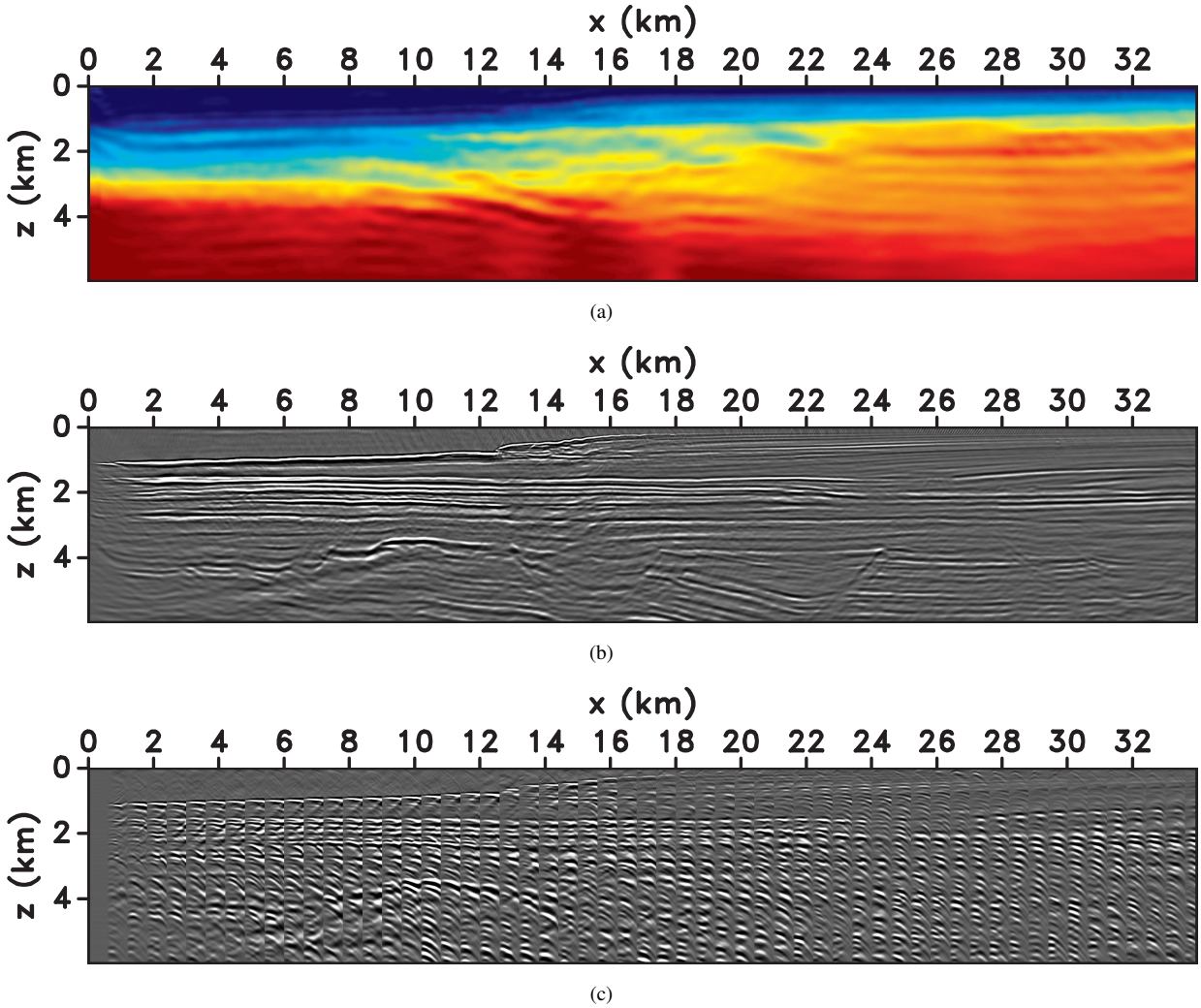


Figure 5. (a) The data-domain wavefield tomography velocity model built from Figure 4(a), (b) corresponding RTM image, and (c) angle-gathers at sparse locations. The velocity ranges from 1.5km/s for water velocity to 4km/s in the deepest part.

the Madagascar open-source software package (Fomel et al., 2013) freely available from http://www.ahay.org.

REFERENCES

Biondi, B., and W. Symes, 2004, Angle-domain common-image gathers for migration velocity analysis by wavefield-continuation imaging: Geophysics, **69**, 1283–1298.

Bunks, C., F. Saleck, S. Zaleski, and G. Chavent, 1995, Multiscale seismic waveform inversion: Geophysics, **60**, 1457–1473.

Dix, C., 1955, Seismic velocities from surface measurements: Geophysics, **20**, 68–86.

Fomel, S., P. Sava, I. Vlad, Y. Liu, and V. Bashkardin, 2013, Madagascar: open-source software project for multidimensional data analysis and reproducible computational experiments: Journal of Open Research Software, **1**, e8.

Gardner, G., L. Gardner, and A. Gregory, 1974, Formation velocity and densitythe diagnostic basics for stratigraphic traps: Geophysics, **39**, 770–780.

Kamei, R., R. G. Pratt, and T. Tsuji, 2013, On acoustic waveform tomography of wide-angle obs data-strategies for preconditioning and inversion: Geophysical Journal International.

Plessix, R.-E., 2006, A review of the adjoint state method for computing the gradient of a functional with geophysical applications: Geophysical Journal International, **167**, 495–503.

Pratt, R., 1999, Seismic waveform inversion in the frequency domain, part 1: Theory and verification in a physical scale model: Geophysics, **64**, 888–901.

Rickett, J. E., and P. C. Sava, 2002, Offset and angle-domain

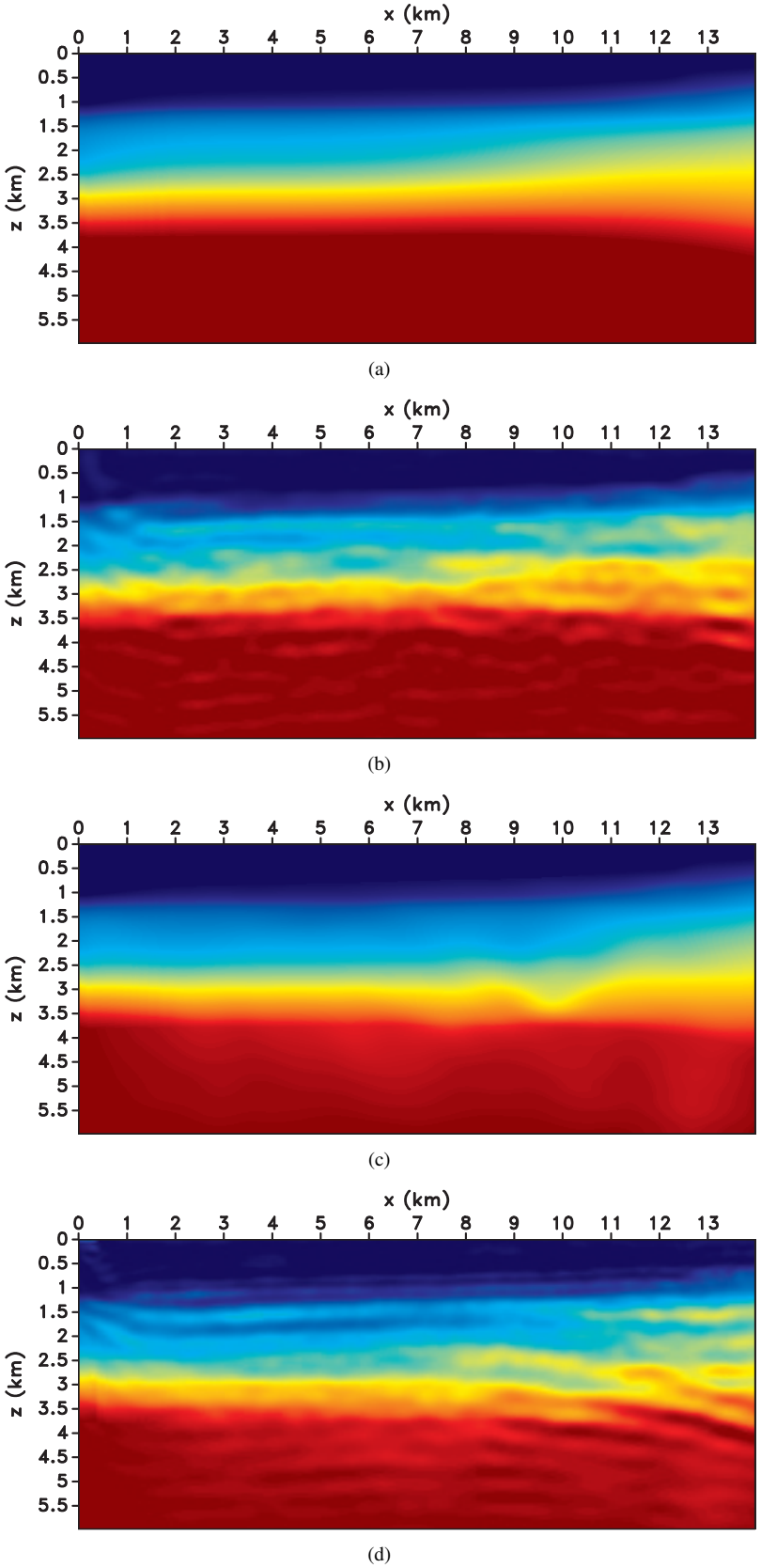


Figure 6. Detail from (a) initial velocity, (b) data-domain wavefield tomography built with initial velocity, (c) image-domain wavefield tomography velocity model, and (d) data-domain wavefield tomography model built with image-domain wavefield tomography model.

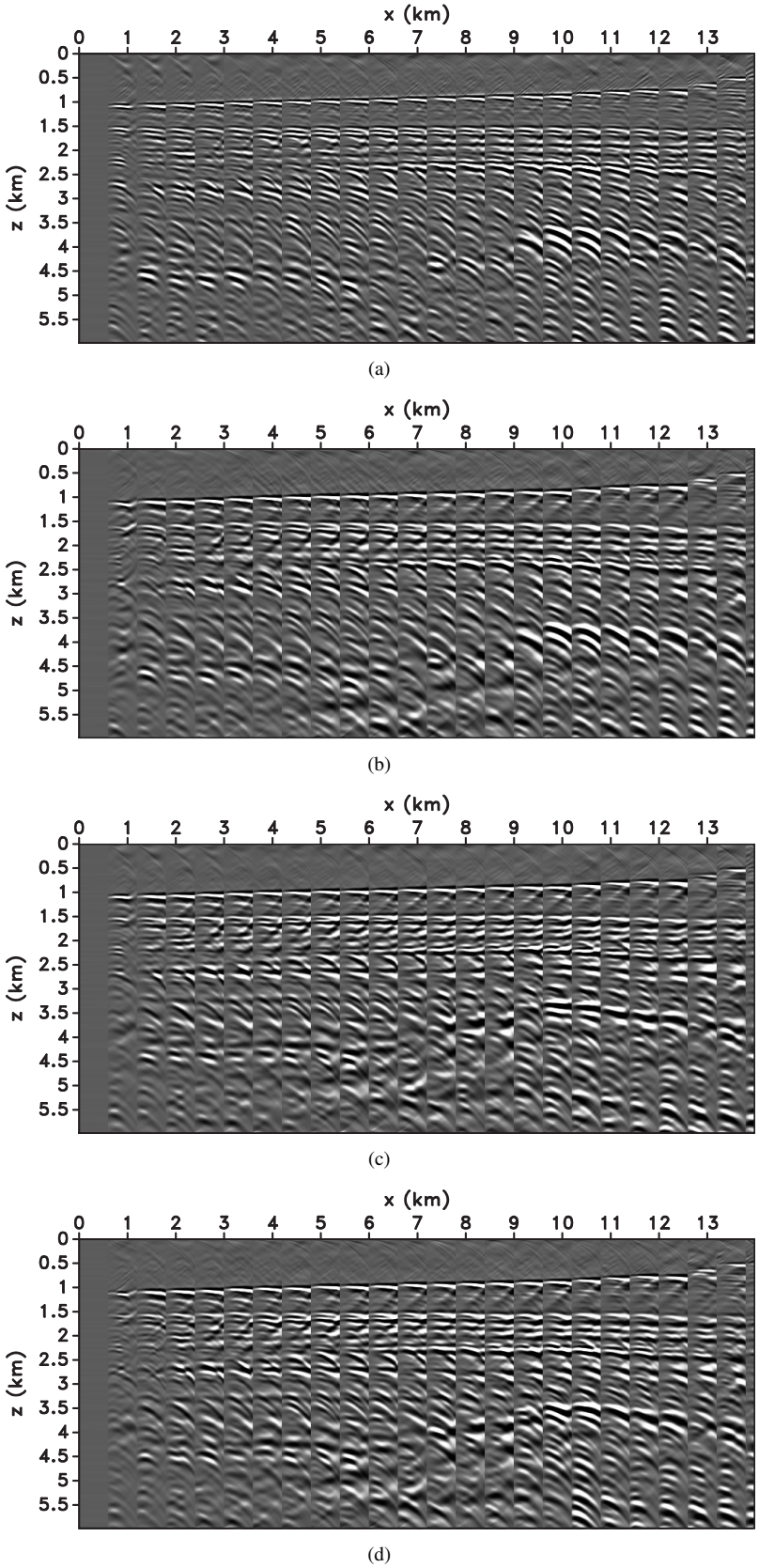
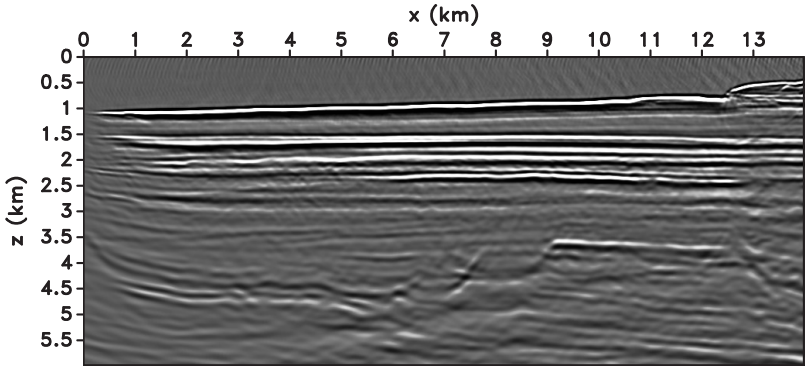
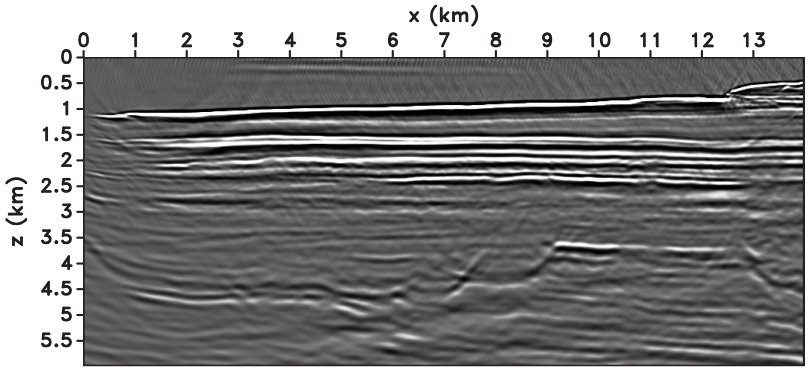


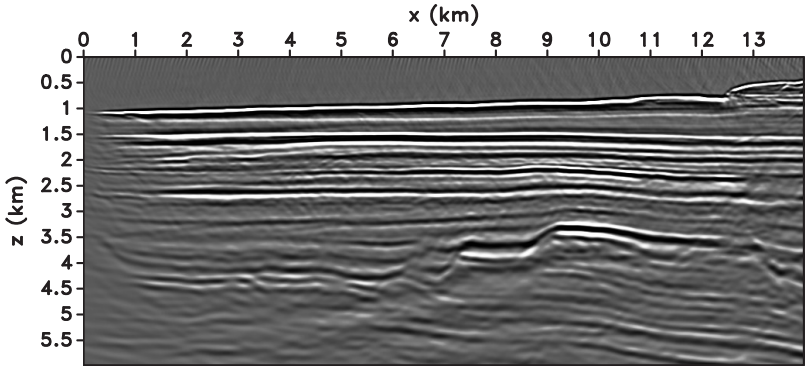
Figure 7. Detail from angle gathers from (a) initial velocity, (b) data-domain wavefield tomography built with initial velocity, (c) image-domain wavefield tomography velocity model, and (d) data-domain wavefield tomography model built with image-domain wavefield tomography model.



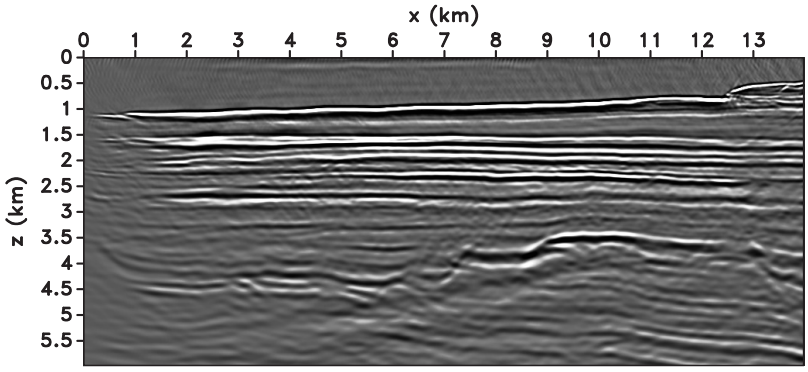
(a)



(b)



(c)



(d)

Figure 8. Detail from RTM images from (a) initial velocity, (b) data-domain wavefield tomography built with initial velocity, (c) image-domain wavefield tomography velocity model, and (d) data-domain wavefield tomography model built with image-domain wavefield tomography model.

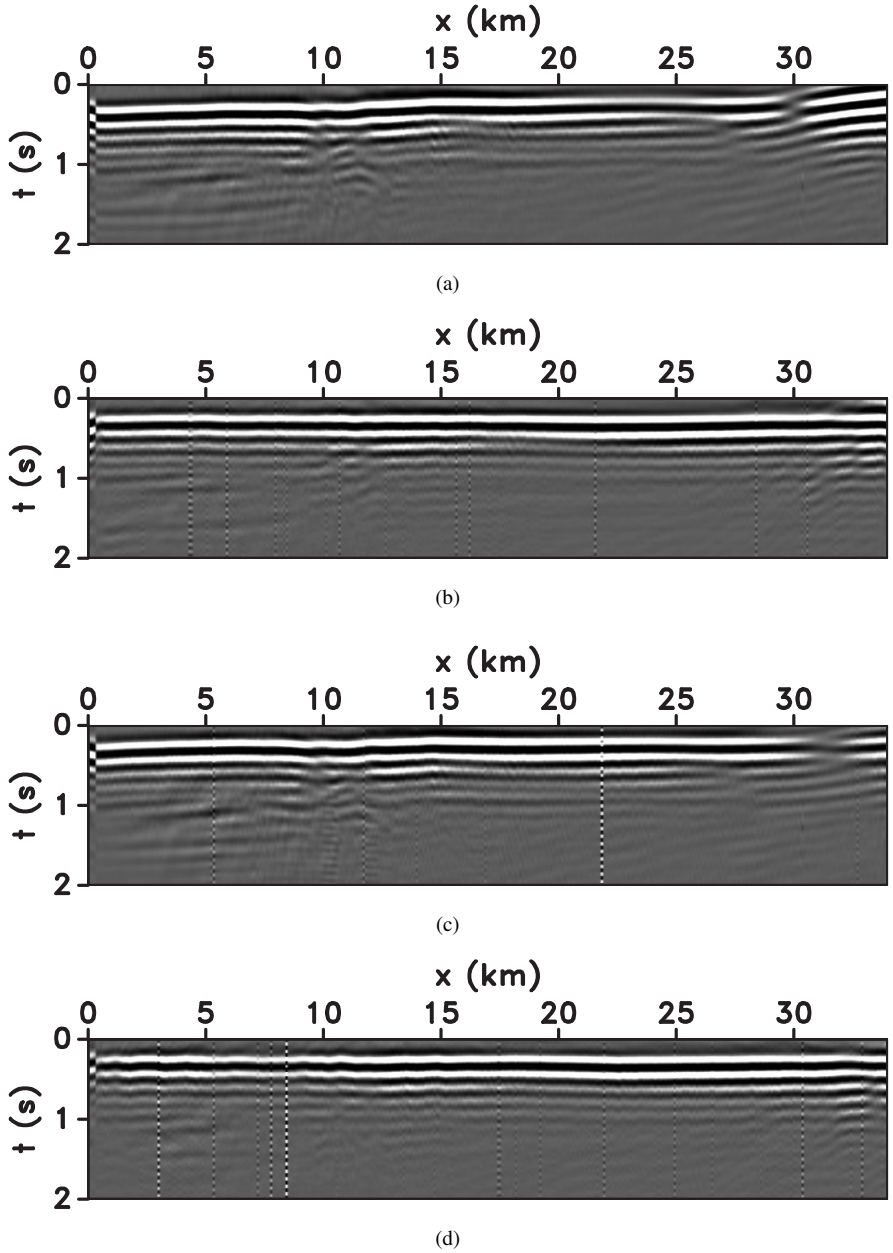


Figure 9. Source inversions as a function of source position: (a) from initial model, (b) from data-domain wavefield tomography using initial model, (c) from image-domain wavefield tomography model, and (d) data-domain wavefield tomography from image-domain wavefield tomography model.

common image-point gathers for shot-profile migration: Geophysics, **67**, 883–889.

Sava, P., and B. Biondi, 2004a, Wave-equation migration velocity analysis - I: Theory: Geophysical Prospecting, **52**, 593–606.

———, 2004b, Wave-equation migration velocity analysis - II: Subsalt imaging examples: Geophysical Prospecting, **52**, 607–623.

Sava, P., and S. Fomel, 2006, Time-shift imaging condition in seismic migration: Geophysics, **71**, S209–S217.

Sava, P., and I. Vasconcelos, 2011, Extended imaging conditions for wave-equation migration: Geophysical Prospecting, **59**, 35–55.

Sava, P. C., and S. Fomel, 2003, Angle-domain common-image gathers by wavefield continuation methods: Geophysics, **68**, 1065–1074.

Shan, G., and Y. Wang, 2013, Rtm based wave equation migration velocity analysis: 4726–4731.

Shen, P., and H. Calandra, 2005, One-way waveform inversion within the framework of adjoint state differential mi-

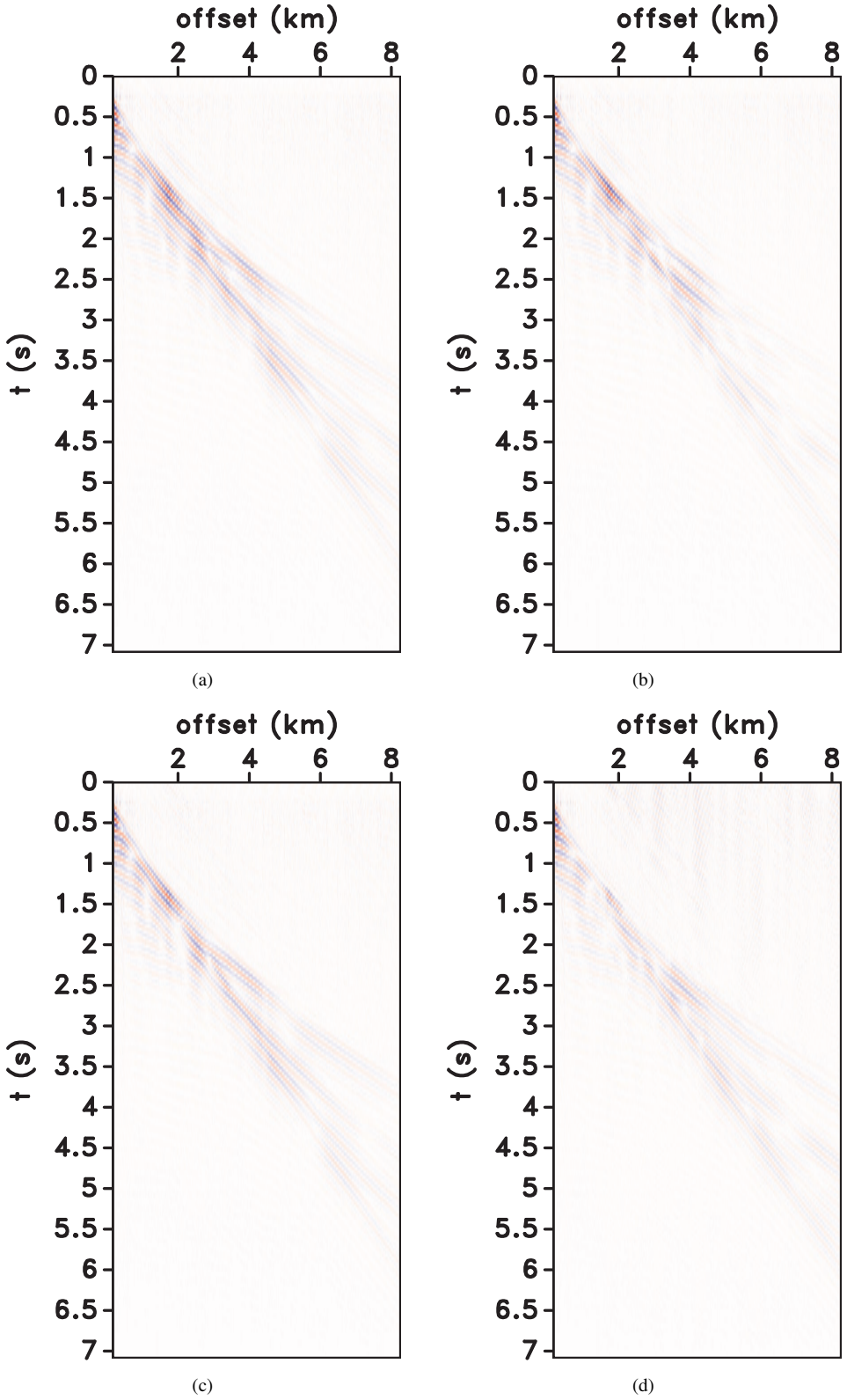


Figure 10. Data domain residuals for shot position $x = 18.75$ km using: (a) the inital velocity model, (b) the data-domain model built from the inital model, (c) the image-domain model, and (d) the data-domain model built from the image-domain model.

gration: 1709–1712.
Shen, P., and W. W. Symes, 2008, Automatic velocity analysis via shot profile migration: Geophysics, **73**, VE49–VE59.
Shin, C., and Y. Ho Cha, 2009, Waveform inversion in the Laplace–Fourier domain: Geophysical Journal International, **177**, 1067–1079.
Sirgue, L., and R. Pratt, 2004, Efficient waveform inversion and imaging: A strategy for selecting temporal frequencies: Geophysics, **69**, 231–248.
Symes, W. W., 2008, Migration velocity analysis and waveform inversion: Geophysical Prospecting, **56**, 765–790.
Tarantola, A., 1984, Inversion of seismic reflection data in the acoustic approximation: Geophysics, **49**, 1259–1266.
Verschuur, D., A. Berkhout, and C. Wapenaar, 1992, Adaptive surfacerelated multiple elimination: Geophysics, **57**, 1166–1177.
Weibull, W., and B. Arntsen, 2013, Automatic velocity analysis with reverse-time migration: Geophysics, **78**, S179–S192.
Woodward, M., 1992, Wave-equation tomography: Geophysics, **57**, 15–26.
Yang, T., and P. Sava, 2010, Wave-equation migration velocity analysis with extended common-image-point gathers.
———, 2011, Image-domain waveform tomography with two-way wave-equation: SEG Technical Program Expanded Abstracts 2011, **508**, 2591–2596.
Yang, T., J. Shragge, and P. Sava, 2013, Illumination compensation for image-domain wavefield tomography: Geophysics, **78**, U65–U76.